SCIENCE CHINA Materials ARTICLES

mater.scichina.com link.springer.com

Published online 31 May 2016 | doi: 10.1007/s40843-016-5059-5
Sci China Mater 2016, 59(5): 337–347

N-doped crumpled graphene: bottom-up synthesis and its superior oxygen reduction performance

Guoxin Zhang[1], Xiuyan Jin[1], Haoyuan Li[1], Lin Wang[1], Cejun Hu[1,2] and Xiaoming Sun[1,2*]

ABSTRACT The crumpled graphene (CrG) was fabricated by applying defluorination of polyvinylidenefluoride (PVDF) on highly curved surface of CaC_2 particle through bottom-up synthetic strategy. The limited reaction depth between PVDF and CaC_2 leads to the formation of CrG with thin layer (3–6 layer graphene) and reasonable high specific surface area (~324.8 m^2 g^{-1}). CrG with N incorporation (N-CrG) was applied as electrode material for reducing oxygen (i.e., oxygen reduction reaction, ORR) in alkaline, showing close onset potential to that of Pt/C and better mass-diffusion behavior. Surprisingly, with increased mass loading of catalysts, N-CrG exhibits steady current increase while Pt/C shows clear current plateau. Meanwhile, the N-CrG sample reveals high cycling stability and tolerance to contaminant, demonstrating its high potential for practical applications. Additionally, the bottom-up synthetic pathway to CrG via polymer dehalogenation on solid alkaline may find more applications which require controlled morphology and thickness of deposited thin graphitic carbon layers.

Keywords: dehalogenation, crumpled graphene, diffusion, oxygen reduction reaction

INTRODUCTION

Electrochemical reducing oxygen holds broad applications in many important processes including fuel cell and metal-air battery [1,2]. Using active catalysts as electrode materials is one common strategy to promote oxygen reduction reaction (ORR), and for this specific purpose, many catalysts of high potential were synthesized, exhibiting highly comparable performance relative to precious Pt [3–5]. Despite the enormous reports on active ORR catalysts, few pay attention onto the packing models of catalytic materials for electrode, while the efficiency of mass transportation especially in ORR was reported to be another key aspect to achieve high performance [6–8]. Commonly, too dense packing or overlap might bury the active sites and lead to insufficient usage of active materials.

Crumpled graphene (CrG), unlike the flat ones, is capable of resisting the restacking of thin layered graphene during processing [9–17]. Thus the devices made by CrG are significantly less dependent on the electrode mass loading, showing high potential of crumpled form in preventing graphene restacking and maintaining high accessible surface area, which is especially appealing for real applications of energy conversion and storage [18–31]. For instance, CrG induced by metal oxide template barely changed its capacitance as current density increasing from 0.5 to 100 A g^{-1}, because the crumpled form can efficiently provide plentiful, stable interfacial contacts and low-electrical-resistance pathways even under extremely high compressive strength [9,15,32,33]. Additionally, the large free volume enclosed by the crumpled thin layers can be utilized for loading active materials and these cargos can be well protected by the inert graphene sheet, which further extends the potential applications [18,21,27,28,34,35]. Currently, the potential-to-scale-up methods are usually based on top-down transforming the 2D graphene sheet into crumpled ball structure while bottom-up synthetic methods remain for exploration [9,33,36]. Top-down technique strictly depended on the water-soluble graphene oxide (GO). Once GO was doped using strategies either solution- or vapor-based [9,27,32], the reduction of GO mostly happened, causing defunctionalization of GO and degradation of the operability of graphene sheet [37–39], which may possibly result in failing of crumpling state. While, it is believed that dopant types could be simply tuned following bottom-up solution-based strategy without crumpled structure compromise, especially for the strategy applying solid templates [40–42].

Here in this study, instead of conventional method for

[1] State Key Laboratory of Chemical Resource Engineering, Beijing 100029, China
[2] College of Energy, Beijing University of Chemical Technology, Beijing 100029, China
[*] Corresponding author (email: sunxm@mail.buct.edu.cn)

CrG fabrication which is top-down from the structuring of GO [20,43], bottom-up strategy was applied to fabricate CrG via localized defluorination of polyvinylidenefluoride (PVDF) at the interfaces with particular CaC_2, as shown in Scheme 1. PVDF was used as the carbon source to wrap CaC_2 particles. Defluorination reaction was induced by the alkalinity of CaC_2 to form few-layered graphene. The final graphene can be bombed/cracked by as-formed C_2H_2 due to the inner remaining CaC_2 reacting with water. Because of the limited reaction depth between PVDF and CaC_2, and also the high melting point of CaC_2, CrG with thin layer (3–6 layers) and highly curved structure was formed. The bottom-up synthetic pathway of CrG applying polymer dehalogenation on solid alkaline has high potential to tailor the layer thickness or the morphology of the as-prepared CrG to meet desirable needs. The resulted CrG had specific surface area (SSA) of 324.8 $m^2 g^{-1}$, even after 900°C annealing. Nitrogen was introduced in the carbon deposition stage using melamine to explore doped graphene of crumpled form for the application of ORR. The annealed CrG samples, taking advantage of its crumpled form, high SSA, and N doping, show excellent ORR performance with high catalyst loading in alkaline electrolyte of 0.1 mol L^{-1} KOH, comparable to 20 wt.% Pt/C. Its crumpled form further allows high catalyst loading for high output current density without triggering large overpotential, which demonstrates its high practical potential.

EXPERIMENTAL

Materials

PVDF was purchased from J&K Scientific Ltd. CaC_2 of grade 1 was obtained from Aladdin chemical Co., Ltd. Melamine and *N*,*N*-dimethylactamide (DMAc) of A.R. grade were purchased from Beijing Chemical Factory and used as received.

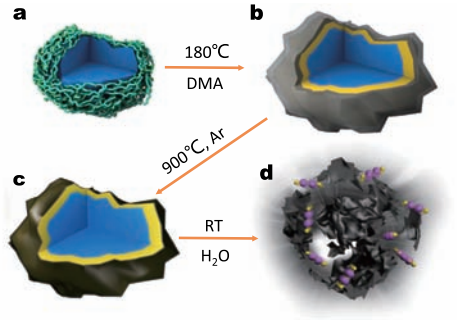

Scheme 1 Graphically depiction of the CrG fabrication through PVDF templated and defunctionalized by irregularly shaped alkaline CaC_2 (blue). The interfacial CaC_2 will transfer to CaF_2 (yellow) but inner CaC_2 would probably stay their initial state of CaC_2 which can be used to generate C_2H_2 (pink) to detonate the annealed product to crack the surficial graphene (black) into small sized CrG.

Bottom-up synthesis of N-doped CrG

CrG was prepared via solvothermal treatment. Typically, 0.64 g PVDF was dissolved in 30 mL DMAc by sonication (~240 kHz), followed by magnetically stirring until a homogeneous solution was formed. Afterwards, 0.50 g melamine was added into the suspension under thorough sonication. After a uniform suspension was formed, 1.0 g fine CaC_2 powder freshly prepared was added into the uniform suspension, followed by a ~10 min magnetically stirring. Eventually, the suspension was transferred to a 40 mL-packed Teflon-lined autoclave and heated at 180°C for 12 h. Primary product was obtained after two cycles of wash with ethanol and 70°C oven dry. Solid precursors were subscribed to inert annealing at 700, 800, and 900°C. Calcined products were poured in dilute HCl solution and sonicated to remove the byproduct CaF_2, followed by thorough washing and 70°C oven dry. The sample annealed at 700, 800, and 900°C were labled as CrG-700/800/900, respectively.

Characterizations

The morphologies and structures of the materials were examined using scanning electron microscopy (SEM) (Zeiss SUPRA 55), transmission electron microscopy (TEM) (Hitachi 800), high resolution TEM (HRTEM) (JEOL JEM-2100). Chemical compositions were tested using X-ray photoelectron spectroscopy (XPS) (Thermo Electron ESCALAB 250). Powder X-ray diffraction (XRD) patterns of samples were recorded on a Shimadzu XRD-6000. Raman spectra were recorded on a LabRAM Aramis Raman spectrometer (HORIBA Jobin Yvon). Nitrogen adsorption/desorption analyses were performed using Quantachrome Instruments (USA) Autosorb-1 at-196°C. Specific surface area was calculated from the adsorption branch according to the Brunauer-Emmett-Teller (BET) method. The pore size distribution plot was derived from the adsorption branch of the isotherm based on the Barrett-Joyner-Halenda (BJH) method.

Electrochemical measurements

5.0 mg catalyst and 10 μL Nafion (DuPont, 5 wt.%) were dispersed in 1.0 mL *N*,*N*-dimethylformamide (DMF) by at least 10 min sonication to form a homogeneous ink. 5.0 μL ink (containing 25.0 μg catalyst) was loaded on a glassy

carbon rotating disk electrode (RDE) of 5 mm in diameter (Pine Instruments) giving a loading of 0.1274 mg cm^{-2}. Cyclic voltammetry (CV) (using PARSTAT 2273 potentiostat from Princeton Applied Research) was conducted in an electrochemical cell using the saturated calomel electrode (SCE) as the reference electrode, a 1.0 cm^2 platinum foil as the counter electrode and the sample modified glassy carbon electrode as the working electrode. The electrolyte (0.1 mol L^{-1} KOH) was saturated with oxygen by bubbling O_2 prior to the measurement. A flow of O_2 was kept over the electrolyte during the data recording. The working electrode was cycled at least 5 times before data were collected with a scanning rate of 50 mV s^{-1}. For the RDE measurements, the working electrode was scanned cathodically with a scanning rate of 5 mV s^{-1} and varied rotating speed from 400 to 2025 rpm. Koutecky-Levich plots (j^{-1} *vs.* $\omega^{-1/2}$) were studied at various electrode potentials. The slopes of the linear fit lines were used to calculate the number of electrons transferred (n) according to the Koutecky-Levich equation [44]:

$$\frac{1}{J} = \frac{1}{J_L} + \frac{1}{J_K} = \frac{1}{B\varpi^{1/2}} + \frac{1}{J_K}, \quad (1)$$

$$B = 0.62nFC_o(D_o)^{2/3}v^{-1/6}, \quad (2)$$

$$J_K = nFkC_o, \quad (3)$$

where J is the measured current density, J_K and J_L are the kinetic- and diffusion-limiting current densities, ω is the angular velocity in rpm, n is the transferred electron number, F is the Faraday constant, C_o is the bulk concentration of O_2, D_o is the O_2 diffusion coefficient, v is the kinematic viscosity of the electrolyte, and k is the electron-transfer rate constant.

For the rotating ring-disk electrode (RRDE) measurements, the catalyst inks and electrodes were prepared by dissolving 5.0 mg solid samples in 500 μL DMF, the catalysts' loading were the same as that in RDE measurements, which was 0.1274 mg cm^{-2}. The ink was dried slowly under infrared light in air and the drying condition was adjusted by trial and error until a homogeneous catalyst distribution across the electrode surface was obtained. The disk electrode was scanned cathodically with a scanning rate of 5 mV s^{-1} and the ring potential was constant at 1.50 V *vs.* reversible hydrogen electrode (RHE). The H_2O_2 percentage and the electron transferred number (n) were determined by the following equations:

$$\%HO_2^- = 200 \times \frac{I_r/N}{(I_d + I_r/N)}, \quad (4)$$

$$n = 4 \times \frac{I_d}{(I_d + I_r/N)}, \quad (5)$$

where I_d is disk current, I_r is ring current, and N is the collection efficiency (0.37) of the Pt ring electrode.

RESULTS AND DISCUSSION

Effective dehalogenation of PVDF was conducted by the high affinity between Ca on CaC_2 and F on PVDF; meanwhile, strong alkalinity of CaC_2 and high polarity of solvent DMF can also facilitate the leaving of F-functionality. As demonstrated in Scheme 1, thin layered carbonization products and the *in situ* generated insoluble CaF_2 will form at the interface and deposit on the highly curved CaC_2 particle surface, which would prevent further reaction between CaC_2 and PVDF, and form a solid replica of the initial CaC_2 morphology with atomic thickness. The CrG precursor, the encapsulating CaF_2 and the inner remaining CaC_2 were purified and subscribed to inert annealing to graphitize the thin carbon layer. After performing annealing, the inner enclosed CaF_2, CaC_2 and a few $Ca(OH)_2$ generated in the drying process can be completely removed by sonication in diluted HCl. During this washing stage, the remaining CaC_2 will react with water to form C_2H_2 gas, which can effectively fragment the templated CrG, leading to the formation of micro-sized CrG. Heteroatom source, for instance, in this study, melamine, can be incorporated into the thin carbon shell formed on CaC_2, which allow us to further explore electrochemical applications of CrG products due to its highly N-doped trait. The irreplaceable role of CaC_2 in the dehalogenation of PVDF was evidenced with controlled experiments using blank or different types of alkaline to defunctionalize PVDF. (Experiments No. 1, 2, 3, 4, and 5 represent for the solvothermal treatments of melamine, PVDF, PVDF/melamine, PVDF/CaC_2, and PVDF/CaC_2/melamine, respectively.) As shown in Fig. S1a, obvious carbonization can be observed from Experiments No. 3, 4, and 5 except the other two, in which organic (melamine) or inorganic (CaC_2) alkaline were involved to defluorinated PVDF. No visual carbonized products were found for solvothermal treatment of solo PVDF or solo melamine which clearly evidenced that no carbonization happened. Furthermore, Experiment No. 3 applying solo organic alkaline of melamine obtained very few solid product even after 10 min centrifugation at 12,000 rpm (Fig. S1c). This limited product was further verified to be dominated by melamine, not originated from carbonization of PVDF, as illustrated in Fig. S2. While for the product of Experiment No. 4 applying inorganic CaC_2, big-sized particles can be found, after dryness. These

particles were characterized presenting large amount of CaF_2 and a few $Ca(OH)_2$ ($Ca(OH)_2$ was generated by CaC_2 reacting with H_2O during washing and drying), matching our abovementioned statements (Fig. S3). After complete removal of soluble components in diluted HCl and further cracked by C_2H_2 gas bubbles, the thin layered CrG was obtained, as revealed in Fig. S4.

In order to demonstrate the feasibility of the bottom-up strategy in fabricating applicable CrG, organic alkaline melamine as well as one common N source was introduced in the solvothermal synthetic condition to co-dehalogenate PVDF and dope the carbon matrix with nitrogen. As shown in Fig. S5, the solvothermal treated suspension (Experiment No. 5) of PVDF/CaC_2/melamine results in particular products with highly curved surface, which was characterized to be dominated by CaF_2. Alike to Experiment No. 4, $Ca(OH)_2$ was formed during the drying process (Fig. S5c). Annealed sample of Experiment No. 5 went through the explosive purification process to form fragmented CrG. The final CrG annealed at 900°C (yield~20.8%) was subscribed to electron microscopy measurements, and revealed to be highly crumpled and even thinner than products from Experiment No. 5, as shown in Fig. 1a. Typical morphology of highly crumpled graphene of CrG-900 (annealed at 900°C), abundant wrinkles and inner voids can be observed. A few enclosed carbon capsules can be also observed in 900°C-annealed CrG, which was formed with the assistance of the *in situ* generated CaF_2 and CaC_2 template, as displayed in Fig. 1b. CrG was substantiated to be highly graphitized, clear crystallized graphene layers can be found and the layers' number falls in 4–6 graphene sheet (Fig. 1b, CrG-700 and CrG-800 are shown in Fig. S6, whose yields are at ~30%), which thanks to the limited reaction depth between PVDF and CaC_2. Fig. 1c shows abundant micropores presenting in CrG-900. Cyclic narrow strip of N_2 adsorption/desorption (A/D) isotherms in the inset of Fig. 1c confirm the presence of mesopores which are indexed to IV type pore according to its A/D isothermal, corresponds to cone- and plate-shape mesopores [20]. The other two CrG samples (i.e., annealed at 700 and 800°C) are also attributed to type IV pore (Fig. S7). Meanwhile, sharp peaks of (002) graphene lattice of XRD profiles (Fig. 1d) and typical graphitization bands of Raman spectra are presenting in all CrG samples (Fig. S8).

Considerable defect was revealed in the N-CrG by Raman spectra (Fig. S8, I_D/I_G~1.09–1.15). The I_D/I_G ratio is comparable to that of the liquid phase exfoliated graphene but much lower than that of the chemically converted graphene oxide even after reduction (I_D/I_G~1.5–2.5), demonstrating the reasonable graphitization degree [20,45,46]. The defect on CrG may provide plentiful active catalytic sites for adsorbing reaction molecules and conveying efficient catalysis. Fig. S9a shows the XPS elemental survey for the CrG samples, revealing the presence of mainly three peaks located at ~ 285, 400, and 533 eV for C1s, N1s, and O1s, respectively. The N content was estimated to be up to 7.2 at.% in the CrG-700, which would decrease to 2.9 at.% for the CrG-900 upon annealing at 900°C (Figs 1e and S9a). More importantly, curve-fitting of the high-resolution XPS N1s peaks (Fig. S9c) indicates up to ~68.9 at.% N in the form of graphitic N, which was reported to be one of the most active catalytic N sites for ORR and could also improve the overall conductivity [16,47–49]. The curve-fitted XPS C1s spectrum of the CrG-900 is given in Fig. 1f, which shows 80.7% graphitic carbon, 18.2% C–N/C–O, and 8.1% C=O. The presence of O-containing groups could enhance the O_2 adsorption while the high content of graphitic N species could act as active sites for ORR. Interestingly, it was found that the control sample of CrG synthesized without melamine still possessed ~1.85 at.% N doping (Fig. S10). Considering the only N source in this case was the solvent of DMAc, we may safely conclude that the *on-site* defluorinated carbon atoms were extremely reactive and could even extract heteroatoms from stable organic molecules [39,50], which further demonstrated the effectiveness of our synthetic strategy for various of doped carbon materials. The morphology of control sample (the sample synthesized without melamine addition was annealed at 900°C and denoted as CrG-9-no-ME) was still crumpled form with thin layers (Fig. S10a). XRD profile (Fig. S10b) reveals the high graphitization degree that CrG-9-no-ME possessed, similar to other CrG samples.

To evaluate the ORR performance of the CrG samples, we fabricated them into electrodes and performed CV and polarization measurements using a RRDE unless otherwise stated. As shown in Fig. 2a, the CrG-900 exhibits a CV with the same onset potential and the maximum current peak relative to that of commercial 20 wt.% Pt/C. Fig. 2b reproduces the linear scanning voltammetry (LSV) curve for the CrG-900, showing a highly comparable onset and even better half-wave potential to those of the Pt/C electrode, but left big gap of limiting current density being much less than that of 20 wt.% Pt/C. The CrG-900 exhibited advanced onset and half-wave potentials than that of the previously reported CrG which made by the conventional top-down methods (Table S1) [51–55]. Fig. 2c reproduces the Tafel plots of the CrG-900 and Pt catalyzing ORR, which was

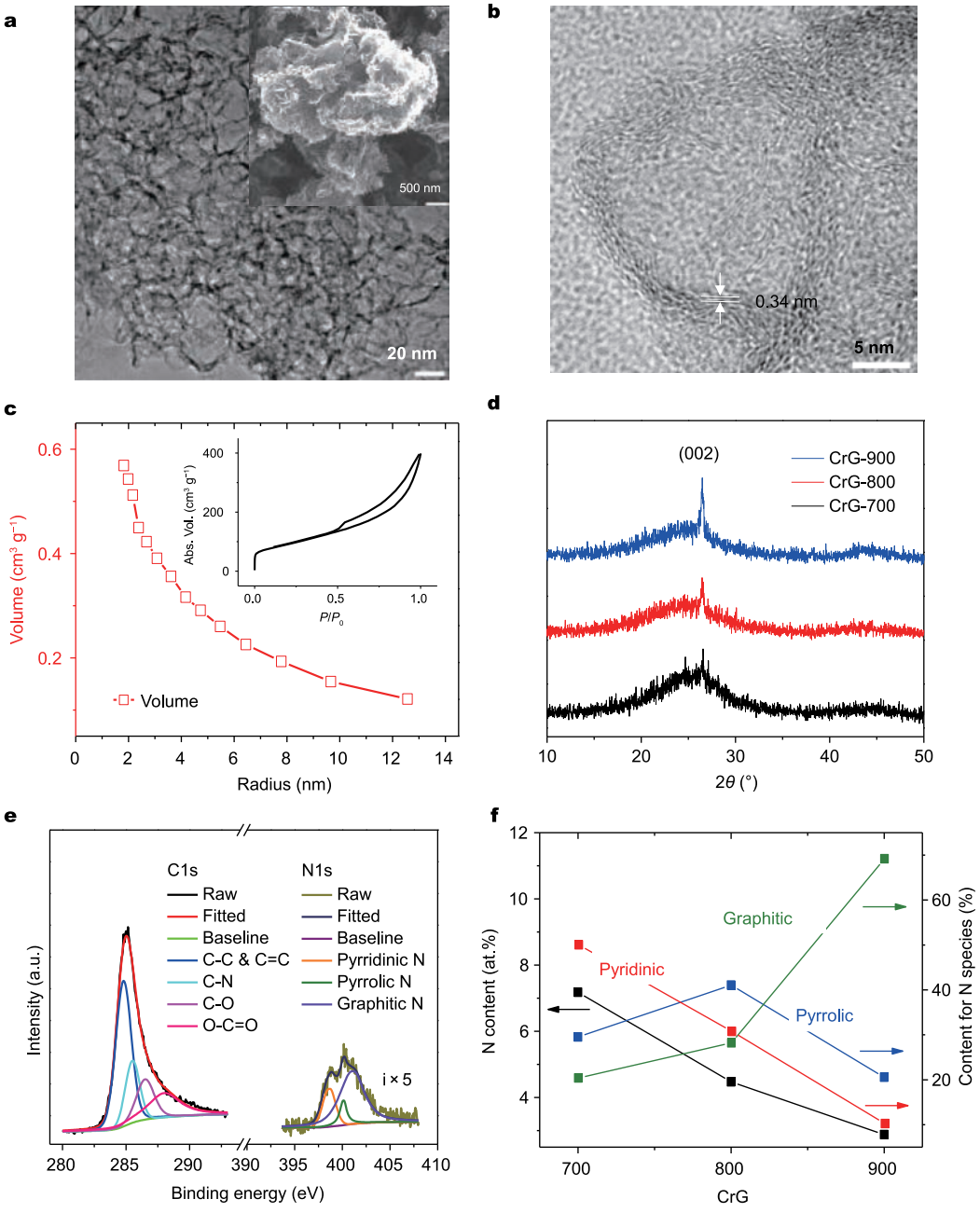

Figure 1 Typical morphology of the CrG which was annealed at 900°C: (a) TEM image, inset shows the SEM image of the CrG-900, in which thin layered and crumpled form can be observed. (b) Manified TEM image of the CrG-900. (c) BET measurements: pore volume of the CrG-900, inset shows the N_2 A/D curve. (d) XRD patterns of the CrG samples. XPS analysis: (e) C1s and (f) N1s spectra of the CrG-900. Graphitic N takes nearly 70% of overall N species.

originated from LSV curves. As implied by the slightly small slope of the CrG-900 (52.2 mV dec^{-1}), it was suggested that the ORR could be facilitated similarly fast on the CrG-900 as it on precious Pt. As shown in Fig. 2d, a diffusion-controlled 4e-ORR process occurs over a wide potential window from 0 to 0.85 V, as the case for the Pt/C electrode. Similar to the Pt/C electrode, the amount H_2O_2 generated is also very low (< 8%, Fig. 2d). Compared with the CrG-900, the CrG-700/800 exhibits bigger cyclic areas (Fig. S11a), presumably due to their higher (O-containing) functionality contents but smaller limiting current densities and lower onset potentials (Fig. S11b, measured on a RDE) associated with the lower contents of graphitic N (Fig. S9c).

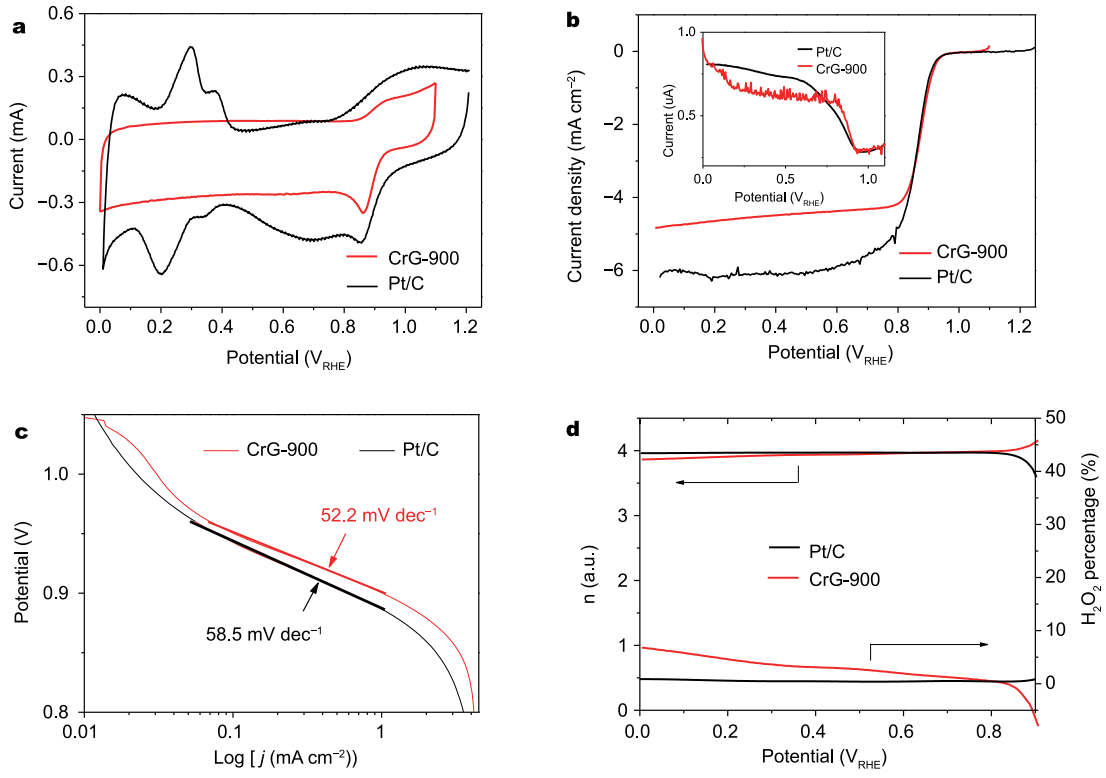

Figure 2 The ORR performance of the CrG-900 (red) relative to the commercial 20 wt.% Pt/C (black). (a) CV; (b) polarization curves (including disk current density and ring current (inset), 1600 rpm-line was selected); (c) Tafel plot of the ORR on CrG-900 and Pt/C catalysts. (d) Electron transfer-ring number and generating H_2O_2 percentage. Catalyst loading=0.3 mg cm^{-2}. All electrochemical measurements abovementioned were conducted in O_2-saturated 0.1 mol L^{-1} KOH electrolyte and copying the 1600 rpm polarization curve of disk (or plus ring) current.

Electrochemical impedance spectroscopy (EIS) is frequently used to investigate the electrode reactions involving mass transportation [56]. The cases with heavy loading catalysts of 0.45 mg cm^{-2} (three fold of catalyst loading on the abovementioned case for activity comparison between Pt and CrG-900) were performed with the EIS measurements. The EIS of CrG-900 collected at 0.8 V *vs.* RHE against that of Pt/C with the same catalyst loading density was displayed in Fig. 3a. At high frequency region, the Pt/C shows bigger system impedance than CrG-900, implying inner resistance increase caused by unavoidably increased contacts between densely packed particles. Due to the nature of high activity of Pt, very small electrochemical reaction semicircle was observed. Thereafter, the EIS comes into the medium frequency where the information of mass/charge transfer resistance and short-region diffusion impedance could be obtained, the impedance could be also called as Warburg resistance [18]. In our cases, Pt exhibits planar electrode behavior and the CrG-900 shows much slower increasing trend which indicates the highly rough surface of the CrG-900 (Fig. 3b) [56]. In low-frequency region, the CrG-900, with mutual supporting crumpled GO sheets, shows much bigger slope than Pt on particle-like carbon, indicating that smooth mass transportation occurs [9,21].

At given rotation rate, it was conceivable that the transportation of the solvated O_2 forced from bulk solution to border of catalyst layer (CL) would be close (schematically shown in Fig. 3c). However, those two cases of CrG-900 and Pt/C are different, for particle-like Pt/C catalyst, densely packed CL was formed, leaving few voids as electrolyte reservoir. When the inner O_2 runs out, it needs to migrate from CL border all the way to the deep CL. While in the CrG-900 case, naturally formed voids and void space between mutual supporting CrG-900 could reserve quite a lot of electrolyte as broad pathways for the solvated O_2 channel and reservoir. When CL is thick and densely loaded with catalyst materials, it is also very hard for ions to penetrate the electrode materials with thin pore structuring, therefore, minor catalysts deep inside the CL would stay inactive due to O_2 deficiency. Providing broad diffusion pathways for the solvated O_2 could be of great significance for the electrode materials free of impact of dense catalyst packing, on one hand, taking full use of CL,

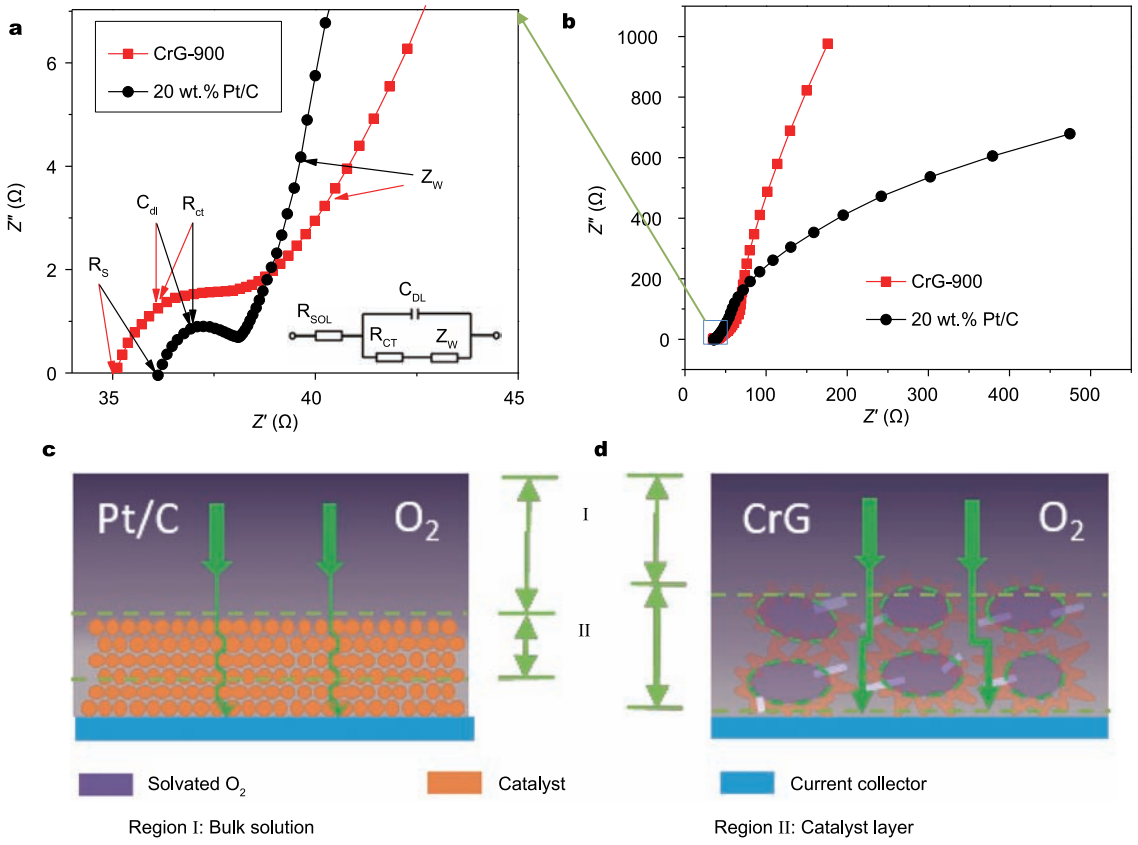

Figure 3 (a) Enlarged part of high frequency region of (b). (b) EIS of electrodes made of Pt/C and CrG-900 at potential=0.8 V (*vs.* RHE). (c) Graphical depiction of the difference of ORR occurring on (a) Pt/C and (b) CrG-900.

on the other hand, achieving high energy of overall devices. The CrG-900 sample holds crumpled morphology which is credited to be beneficial for mass transportation.

In order to obtain high energy of fuel cells or metal-O_2 battery for actual use, sufficiently high density of catalyst loading should be performed to counter the whole package including current collector, electrolyte, separator, and wrappings. Fig. 2a displays high ORR performance of Pt/C catalyst with low catalyst loading of 0.15 mg cm^{-2}; however, the considered aspects especially the limiting current densities show minor advances or even fading after the loading areal density slightly increased over 0.25 mg cm^{-2} (Fig. 4a). While on the contrary, the CrG-900 sample with crumpled morphology, capable of reserving channels for ion passing at very high catalyst loading density, as tested by EIS, suffers no such heavy adverseness, and shows unstopped increase of current density until areal density of catalyst loading reaching as high as 0.75 mg cm^{-2}, as shown in Fig. 4b. Remarkably, the current density of CrG electrode with catalyst loading reaching 0.60 mg cm^{-2}, surpasses that of Pt/C with a 0.35 mA cm^{-2} (Fig. 4c) at low overpotential of 430 mV (U=0.8 V), which highlights the advantages of the structure of crumpled N-doped CrG.

To investigate the stability of the CrG electrode toward ORR and MeOH tolerance, we carried out chronoamperometric measurements at a constant voltage of 0.6 V (*vs.* RHE) within the diffusion-controlled region. As shown in Fig. 5a, the CrG-900 electrode exhibits a significantly better long-term stability than the commercial Pt/C catalyst. In Fig. 5b, the CrG-900 electrode is almost free from the methanol crossover effect whereas a significant variation of CV profile and a considerable activity variation in the ORR performance happened with the Pt/C electrode. Therefore, the CrG-900 fabricated following our newly developed bottom-up synthetic strategy is of high practical importance.

CONCLUSIONS

In summary, a bottom-up synthetic strategy of CrG was developed applying defluorination of PVDF on highly curved surface of CaC_2 particle. Following this strategy, the CrG with thin layer (3–6 layer graphene) and large specific surface area (~324.8 m^2 g^{-1}) was obtained. Layer thickness

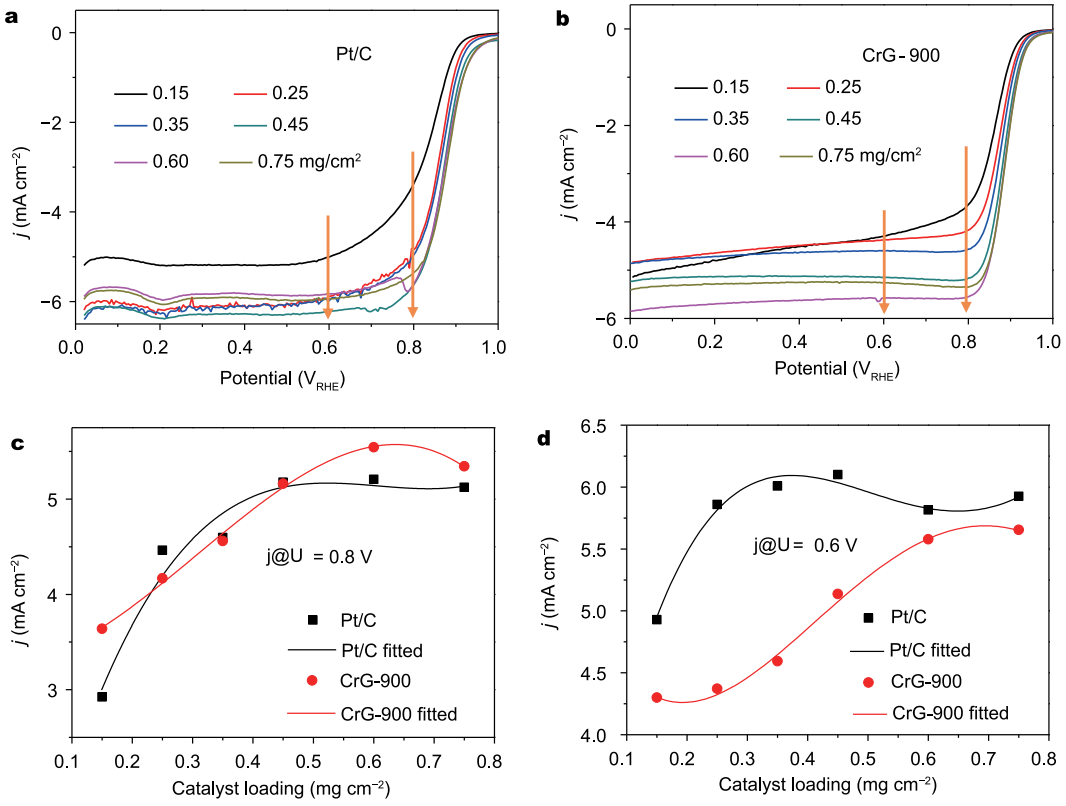

Figure 4 Investigations of the effect of catalyst's loading amount on ORR performance: (a) 20 wt.% Pt/C and (b) CrG-900. The data point of current density at given potential of (c) 0.8 V and (d) 0.6 V. All the polarization curves were collected with 1600 rpm rotation speed.

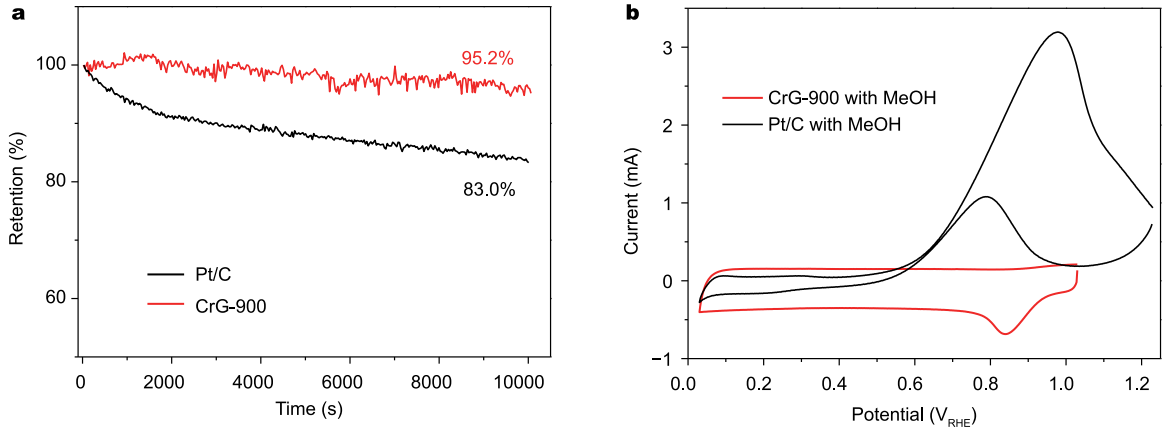

Figure 5 (a) The cycling stability and (b) test of tolerance to methanol.

can be controlled due to the limited reaction depth between PVDF and CaC_2. The CrG-900 with N dopant and crumpled form was applied as electrode material for reducing oxygen in alkaline. Thanks to the structure of crumpled morphology which forms lots of voids inside and between CrG, the solvated O_2 transportation can be greatly facilitated, leading to the current density of the CrG-900 increasing along with the increase of areal density of catalyst loading. Remarkably, at lower overpotential of 0.43 V and loading density of 0.60 mg cm^{-2}, the current density of CrG surpasses that of Pt with 0.35 mA cm^{-2}. Moreover, much higher cycling stability and tolerance to contaminant are observed for N-doped CrG-900, demonstrating high potentials of CrG for practical applications. Additionally, the

bottom-up synthetic pathway to the CrG via polymer dehalogenation by solid alkaline may find more applications in controlling morphology and thickness of deposited thin graphitic carbon layers.

Received 28 April 2016; accepted 24 May 2016; published online 31 May 2016

1 Wu G, Santandreu A, Kellogg W, *et al.* Carbon nanocomposite catalysts for oxygen reduction and evolution reactions: From nitrogen doping to transition-metal addition. Nano Energy, 2016, doi: 10.1016/j.nanoen.2015.12.032
2 Zhang T, Tao Z, Chen J. Magnesium–air batteries: from principle to application. Mater Horiz, 2014, 1: 196–206
3 Dai L, Xue Y, Qu L, *et al.* Metal-free catalysts for oxygen reduction reaction. Chem Rev, 2015, 115: 4823–4892
4 Zhang J, Dai L. Heteroatom-doped graphitic carbon catalysts for efficient electrocatalysis of oxygen reduction reaction. ACS Catal, 2015, 5: 7244–7253
5 Elumeeva K, Fechler N, Fellinger TP, *et al.* Metal-free ionic liquid-derived electrocatalyst for high-performance oxygen reduction in acidic and alkaline electrolytes. Mater Horiz, 2014, 1: 588–594
6 Jang HD, Kim SK, Chang H, *et al.* Three-dimensional crumpled graphene-based platinum–gold alloy nanoparticle composites as superior electrocatalysts for direct methanol fuel cells. Carbon, 2015, 93: 869–877
7 Dai L. Functionalization of graphene for efficient energy conversion and storage. Acc Chem Res, 2013, 46: 31–42
8 Kim JY, Lim J, Jin HM, *et al.* 3D tailored crumpling of block-copolymer lithography on chemically modified graphene. Adv Mater, 2016, 28: 1591–1596
9 Luo J, Jang HD, Huang J. Effect of sheet morphology on the scalability of graphene-based ultracapacitors. ACS Nano, 2013, 7: 1464–1471
10 Zang J, Ryu S, Pugno N, *et al.* Multifunctionality and control of the crumpling and unfolding of large-area graphene. Nat Mater, 2013, 12: 321–325
11 Cranford SW, Buehler MJ. Packing efficiency and accessible surface area of crumpled graphene. Phys Rev B, 2011, 84:
12 Baimova A, Korznikova EA, Dmitriev SV, *et al.* Review on crumpled graphene: unique mechnical properties. Rev Adv Mater Sci, 2014, 39: 69
13 Lin Z, Waller GH, Liu Y, *et al.* 3D Nitrogen-doped graphene prepared by pyrolysis of graphene oxide with polypyrrole for electrocatalysis of oxygen reduction reaction. Nano Energy, 2013, 2: 241–248
14 Xiao L, Damien J, Luo J, *et al.* Crumpled graphene particles for microbial fuel cell electrodes. J Power Sources, 2012, 208: 187–192
15 Guo F, Creighton M, Chen Y, *et al.* Porous structures in stacked, crumpled and pillared graphene-based 3D materials. Carbon, 2014, 66: 476–484
16 Zhang C, Hao R, Liao H, *et al.* Synthesis of amino-functionalized graphene as metal-free catalyst and exploration of the roles of various nitrogen states in oxygen reduction reaction. Nano Energy, 2013, 2: 88–97
17 Deng S, Berry V. Wrinkled, rippled and crumpled graphene: an overview of formation mechanism, electronic properties, and applications. Mater Today, 2016, 19: 197–212
18 Smith AJ, Chang YH, Raidongia K, *et al.* Molybdenum sulfide supported on crumpled graphene balls for electrocatalytic hydrogen production. Adv Energy Mater, 2014, 4: 59–62
19 Lee JY, Lee KH, Kim YJ, *et al.* Sea-urchin-inspired 3D crumpled graphene balls using simultaneous etching and reduction process for high-density capacitive energy storage. Adv Funct Mater, 2015, 25: 3606–3614
20 Wen Z, Wang X, Mao S, *et al.* Crumpled nitrogen-doped graphene nanosheets with ultrahigh pore volume for high-performance supercapacitor. Adv Mater, 2012, 24: 5610–5616
21 Du FH, Liu YS, Long J, *et al.* Incorporation of heterostructured Sn/SnO nanoparticles in crumpled nitrogen-doped graphene nanosheets for application as anodes in lithium-ion batteries. Chem Commun, 2014, 50: 9961–9964
22 An C, Wang Y, Li L, *et al.* Effects of highly crumpled graphene nanosheets on the electrochemical performances of pseudocapacitor electrode materials. Electrochim Acta, 2014, 133: 180–187
23 Mao S, Wen Z, Huang T, *et al.* High-performance bi-functional electrocatalysts of 3D crumpled graphene–cobalt oxide nanohybrids for oxygen reduction and evolution reactions. Energy Environ Sci, 2014, 7: 609–616
24 Liu YZ, Chen CM, Li YF, *et al.* Crumpled reduced graphene oxide by flame-induced reduction of graphite oxide for supercapacitive energy storage. J Mater Chem A, 2014, 2: 5730–5737
25 Zou Y, Kinloch IA, Dryfe RAW. Nitrogen-doped and crumpled graphene sheets with improved supercapacitance. J Mater Chem A, 2014, 2: 19495–19499
26 Wang Y, Wu Y, Huang Y, *et al.* Preventing graphene sheets from restacking for high-capacitance performance. J Phys Chem C, 2011, 115: 23192–23197
27 Luo J, Zhao X, Wu J, *et al.* Crumpled graphene-encapsulated si nanoparticles for lithium ion battery anodes. J Phys Chem Lett, 2012, 3: 1824–1829
28 Choi SH, Lee JK, Kang YC. Three-dimensional porous graphene-metal oxide composite microspheres: preparation and application in Li-ion batteries. Nano Res, 2015, 8: 1584–1594
29 Yan J, Xiao Y, Ning G, *et al.* Facile and rapid synthesis of highly crumpled graphene sheets as high-performance electrodes for supercapacitors. RSC Adv, 2013, 3: 2566–2571
30 Zang J, Cao C, Feng Y, *et al.* Stretchable and high-performance supercapacitors with crumpled graphene papers. Sci Rep, 2014, 4: 6492
31 Wen G, Wu S, Li B, *et al.* Active sites and mechanisms for direct oxidation of benzene to phenol over carbon catalysts. Angew Chem Int Ed, 2015, 54: 4105–4109
32 Luo J, Jang HD, Sun T, *et al.* Compression and aggregation-resistant particles of crumpled soft sheets. ACS Nano, 2011, 5: 8943–8949
33 Mao S, Wen Z, Kim H, *et al.* A general approach to one-pot fabrication of crumpled graphene-based nanohybrids for energy applications. ACS Nano, 2012, 6: 7505–7513
34 Wang H, Yang Y, Liang Y, *et al.* Graphene-wrapped sulfur particles as a rechargeable lithium–sulfur battery cathode material with high capacity and cycling stability. Nano Lett, 2011, 11: 2644–2647
35 Jang HD, Kim SK, Chang H, *et al.* Three-dimensional crumpled graphene-based platinum–gold alloy nanoparticle composites as superior electrocatalysts for direct methanol fuel cells. Carbon, 2015, 93: 869–877
36 Wang X, Maeda K, Thomas A, *et al.* A metal-free polymeric photocatalyst for hydrogen production from water under visible light. Nat Mater, 2008, 8: 76–80
37 Luo D, Zhang G, Liu J, *et al.* Evaluation criteria for reduced graphene oxide. J Phys Chem C, 2011, 115: 11327–11335
38 Zhang G, Xu Y, Wang L, *et al.* Rational design of graphene oxide and its hollow CoO composite for superior oxygen reduction reaction. Sci China Mater, 2015, 58: 534–542

39 Zhang G, Zhou K, Xu R, *et al.* An alternative pathway to water soluble functionalized graphene from the defluorination of graphite fluoride. Carbon, 2016, 96: 1022–1027
40 Ning G, Xu C, Zhu X, *et al.* MgO-catalyzed growth of N-doped wrinkled carbon nanotubes. Carbon, 2013, 56: 38–44
41 Fan Z, Liu Y, Yan J, *et al.* Template-directed synthesis of pillared-porous carbon nanosheet architectures: high-performance electrode materials for supercapacitors. Adv Energy Mater, 2012, 2: 419–424
42 Ning G, Xu C, Hao L, *et al.* Ferromagnetism in nanomesh graphene. Carbon, 2013, 51: 390–396
43 Parviz D, Metzler SD, Das S, *et al.* Tailored crumpling and unfolding of spray-dried pristine graphene and graphene oxide sheets. Small, 2015, 11: 2661–2668
44 Liu Z, Zhang G, Lu Z, *et al.* One-step scalable preparation of N-doped nanoporous carbon as a high-performance electrocatalyst for the oxygen reduction reaction. Nano Res, 2013, 6: 293–301
45 Luo D, Zhang G, Liu J, *et al.* Evaluation criteria for reduced graphene oxide. J Phys Chem C, 2011, 115: 11327–11335
46 Ding Y, Sun X, Zhang L, *et al.* Entrapping an ionic liquid with nanocarbon: the formation of a tailorable and functional surface. Angew Chem Int Ed, 2015, 54: 231–235
47 Wang DW, Su D. Heterogeneous nanocarbon materials for oxygen reduction reaction. Energy Environ Sci, 2014, 7: 576–591
48 Geng D, Chen Y, Chen Y, *et al.* High oxygen-reduction activity and durability of nitrogen-doped graphene. Energy Environ Sci, 2011, 4: 760–764
49 Lai L, Potts JR, Zhan D, *et al.* Exploration of the active center structure of nitrogen-doped graphene-based catalysts for oxygen reduction reaction. Energy Environ Sci, 2012, 5: 7936–7942
50 Zhang G, Wang L, Hao Y, *et al.* Unconventional carbon: alkaline dehalogenation of polymers yields N-doped carbon electrode for high-performance capacitive energy storage. Adv Funct Mater, 2016, 26: 3340–3348
51 Wang M, Wang J, Hou Y, *et al.* N-doped crumpled graphene derived from vapor phase deposition of PPy on graphene aerogel as an efficient oxygen reduction reaction electrocatalyst. ACS Appl Mater Interfaces, 2015, 7: 7066–7072
52 Jin J, Pan F, Jiang L, *et al.* Catalyst-free synthesis of crumpled boron and nitrogen Co-doped graphite layers with tunable bond structure for oxygen reduction reaction. ACS Nano, 2014, 8: 3313–3321
53 Liu Y, Li J, Li W, *et al.* Nitrogen-doped graphene aerogel-supported spinel CoMn2O4 nanoparticles as an efficient catalyst for oxygen reduction reaction. J Power Sources, 2015, 299: 492–500
54 Wang J, Ma R, Zhou Z, *et al.* Magnesiothermic synthesis of sulfur-doped graphene as an efficient metal-free electrocatalyst for oxygen reduction. Sci Rep, 2015, 5: 9304
55 Mao S, Wen Z, Huang T, *et al.* High-performance bi-functional electrocatalysts of 3D crumpled graphene–cobalt oxide nanohybrids for oxygen reduction and evolution reactions. Energy Environ Sci, 2014, 7: 609–616
56 Srivastava A, Balasubramaniam R. Electrochemical impedance spectroscopy study of surface films formed on copper in aqueous environments. Mater Corrosion, 2005, 56: 611–618

Acknowledgments This work was supported by the National Natural Science Foundation of China, the Program for Changjiang Scholars and Innovative Research Team in the University, and the Fundamental Research Funds for the Central Universities. This work was also supported by the long-term subsidy mechanism from the Ministry of Finance and the Ministry of Education of PRC. We thank Prof. Liming Dai for useful talk and his help in polishing the manuscript.

Author contributions Zhang G designed the experiments; Zhang G, Jin X, Li H and Wang L performed the experiments and the characterizations. Hu C helped in the sample characterization. Zhang G wrote the paper with support from Sun X. All authors contributed to the general discussion.

Conflict of interest The authors declare that they have no conflict of interest.

Supplementary information Supporting data are available in the online version of this paper.

Guoxin Zhang obtained his BE degree of applied chemistry in 2010 in the College of Science, Beijing University of Chemical Technology. Now he is a PhD candidate of chemistry in the same institute. His interests include the synthesis, structuring and compositing of porous carbon materials and layer materials as well as the investigation on their electrical and electrochemical properties.

Xiaoming Sun was born in Pingdu, Shandong Province, China. He gained his BSc and PhD degrees in the Department of Chemistry, Tsinghua University in 2000 and 2005, respectively. After post-doctoral work in Prof. Hongjie Dai's group at Stanford University, he joined the faculty of Beijing University of Chemical Technology in 2008. His research interests focus on the controlled synthesis, separation and assembly of functional inorganic nanomaterials and carbon materials; structure and property regulation of metal oxide arrays.

氮掺杂褶皱石墨烯的自下而上制备及其氧气还原反应研究

张国新[1], 金秀彦[1], 李昊远[1], 王琳[1], 胡策军[1,2], 孙晓明[1,2*]

摘要 本文首次报道了自下而上液相合成褶皱石墨烯, 所使用的制备方法为: 卤化高分子聚偏二氟乙烯(PVDF)在崎岖的强碱CaC_2表面进行脱官能团碳化. 因PVDF的官能团脱除需要CaC_2的存在, 导致二者的界面反应深度受限, 故经由CaC_2脱官能团并模板得到的褶皱薄层碳材料的厚度非常小, 继续高温焙烧可将薄层碳转化为寡层(3~6层)石墨烯, 通过BET测试分析所得到的褶皱石墨烯(CrG)在900°C下焙烧具有高达~324.8 $m^2 g^{-1}$的比表面积. 经过N掺杂修饰的CrG应用于电化学催化氧气还原反应(ORR), 发现其具有和商用铂碳催化剂(20 wt.% Pt/C)相当的起峰电位和半波电位, 且具有更为优秀的促进载荷物质在其孔道内的输运行为. 更为有趣的是: 通过增加催化剂的负载量, N掺杂的CrG表现出极限电流的稳定增加, 而Pt催化剂无此行为, 这种特性可潜在提供给整装器件更高密度的比能量.